Densification of Carbon Nanotubes During Growth

Ahmed Obaid M Alzahrani (aualzahrani@kau.edu.sa)
King Abdulaziz University
Meshari Alayash
King Abdulaziz University
Salem Alghamdi
King Abdulaziz University

Research Article

Keywords: plasma-enhanced, Carbon nanotubes, vapor deposition, qualitative investigation

Posted Date: September 20th, 2021

DOI: https://doi.org/10.21203/rs.3.rs-828997/v1

Densification of carbon nanotubes during growth

Ahmed Obaid M Alzahrani[1,2*], *Meshari Alayash*[1], *Salem Alghamdi*[2]

[1] Center of Nanotechnology, King Abdulaziz University, Jeddah, Saudi Arabia

[2] Physics Department, Faculty of Science, King Abdulaziz University, Jeddah, Saudi Arabia

*Corresponding author: aualzahrani@kau.edu.sa; Tel: 00966566453028.

ABSTRACT: Carbon nanotubes are highly attractive for research purposes due to their field emission properties. However, when the nanotubes are vertically aligned on a substrate to form a continuous film, screening effect is observed, which reduces the efficiency. To densify the tubes into bundles and eliminate this screening effect, costly lithography patterning of catalysts and post-growth chemical treatments have been previously reported. In this work, we report a novel, cheap, and reproducible technique of densifying the growth of carbon nanotubes by utilizing a colloidal catalyst and microwave plasma-enhanced chemical vapor deposition. A qualitative investigation was carried out, and a possible densification mechanism was proposed.

INTRODUCTION

Since the famous experiment by Iijima in 1991 [1], research on carbon nanotubes (CNTs) covering their growth mechanisms, properties, and applications have been carried out tremendously [2]. Due to their superb mechanical [3], optical [4], and electrical properties [5], CNTs have practical and commercial applications in several fields [5]. An application in high demand is electron field emission devices requiring high-density flow of electrons [6]. Field emitters play a crucial role in several essential industries such as display screens [7], X-ray sources [8], and electron guns [9].

An array of vertically aligned multiwall CNTs (MW-CNTs) can function as electron field emitters. Nevertheless, when they are arranged in the form of a continuous uniform film, the screening effect reduces the efficiency of the device [10]. Consequently, an isolated CNT can produce a larger field emission current than one embedded in a large "forest" of CNTs [11]. To overcome this drawback, lithography has been utilized to attain patterned CNTs by precisely controlling the catalyst spacing [12]. However, such a process is expensive and time-consuming, especially if a relatively large sample area (of the order of cm^2) is required. An alternative technique based on the post-treatment of CNT films is used to form local assembly of the tubes, using either dry [13] or liquid [14] densification. In the former, the CNT bundles are sealed with a silicon oxide coating under low pressure, and densification occurs due to a sudden pressure change when the chamber is vented [13]. However, this requires patterned CNT bundles prepared using lithographical techniques as the first step. A number of other studies used liquid densification with ethanol [14] and acids [15]. Nonetheless, such chemical processes might also etch the nanotubes and affect their electrical properties negatively.

Here, we report a simpler, novel method to densify CNTs into bundles during their growth. A qualitative investigation was carried out to observe and analyze experimental results, and a possible interpretation is discussed here.

RESULTS AND DISCUSSION

Fe_3O_4 nanoparticles and their deposition on substrate. In this work, iron oxide nanoparticles were synthesized by thermal decomposition of iron carbonyl in a solvent with a high boiling point. [16] Fig. **1** shows two transmission electron microscopy (TEM) images of the obtained nanoparticles. Despite the sonication process in hexane, large aggregates of particles approximately 1 μm in size (indicated with yellow arrows in Fig. 1a) still existed. Figure 1b indicates particles of almost same sizes, which were separated from each other due to the use of oleic acid as a surfactant. The high-magnification image (Fig. 2) clearly shows the shape of the iron oxide nanoparticles with an average size of approximately 20 nm. The inset in Fig. 2 indicates an inter-plane spacing of 0.258 nm that corresponds to the (3 1 1) planes in Fe_3O_4 [17]. To investigate the crystalline structure and phase of the particles, their X-ray diffraction (XRD) pattern was collected employing the powder mode setup. The obtained pattern (Fig. 3) shows diffraction peaks corresponding to Fe_3O_4 in the covered range (PDF-Card no. 00-001-1111). Another effective and complementary method to confirm the phase of iron oxide nanoparticles is Raman scattering as all the phases of iron oxides and iron oxyhydroxides exhibit distinct Raman spectra [18]. Fig. 4 shows the Raman spectrum of Fe_3O_4 nanoparticles under 532 nm excitation, where the strong peak at 665 cm^{-1} and a small peak at 542 cm^{-1} agreed with the reported spectrum of magnetite [18].

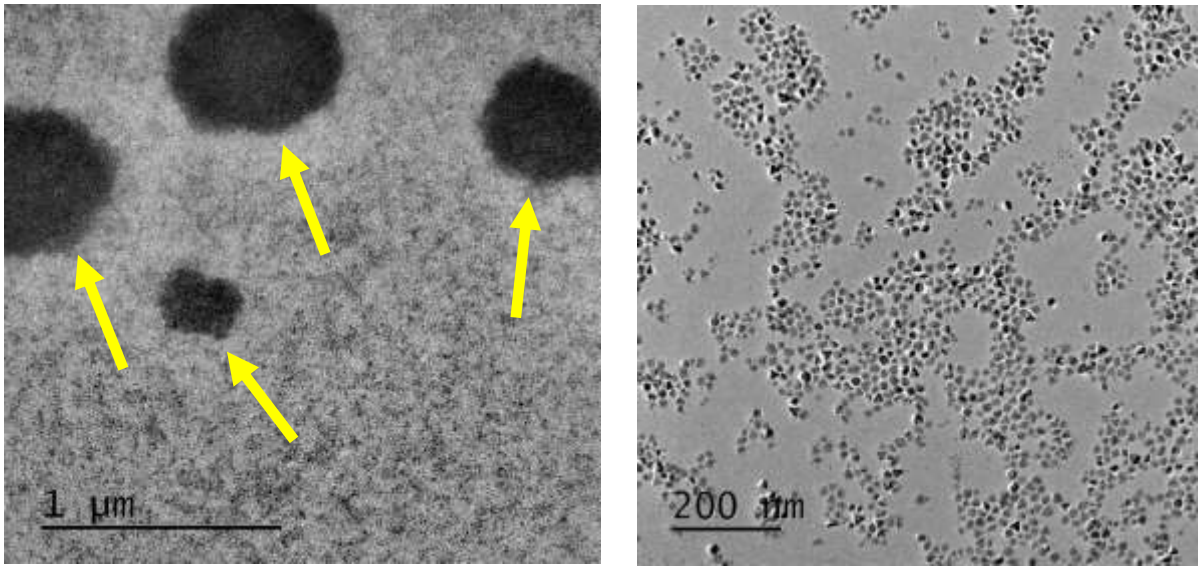

(a) (b)

Fig. 1 TEM images of iron oxide nanoparticles at different magnifications.

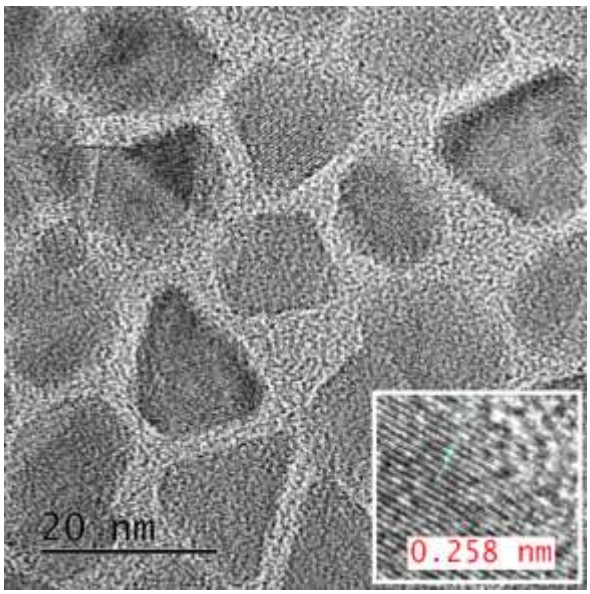

Fig. 2 High-resolution TEM image of Fe_3O_4 nanoparticles. The inset shows the d-spacing corresponding to the (3 1 1) planes.

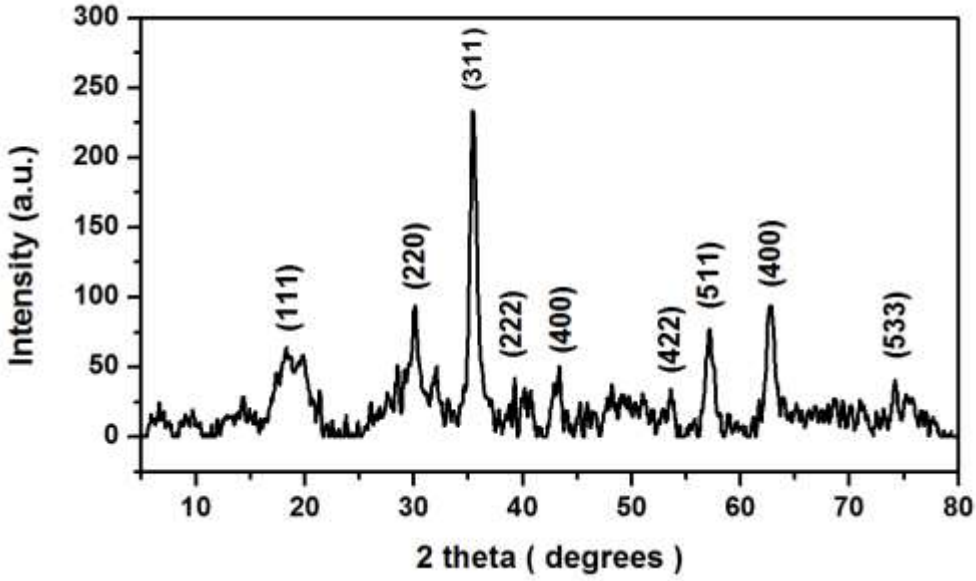

Fig. 3 XRD pattern of the as-prepared Fe_3O_4 nanoparticle powder. The peaks are labeled with the corresponding Millar indices.

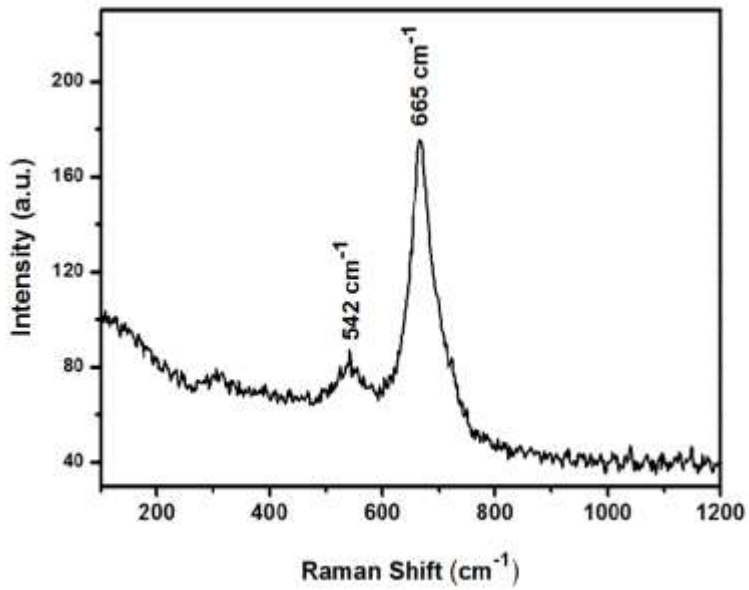

Fig. 4 Raman spectrum of H_2 plasma-treated Fe_3O_4 nanoparticles using 532 nm excitation.

As mentioned in the experimental section, a commercially available Ti-coated stainless steel was placed at the beaker bottom, and a colloidal catalyst particle suspension was poured until reaching ~1 mm above the substrate surface. After the solvent evaporated at room temperature, a high-temperature treatment was still needed to completely eliminate the organic material. However, the heating must be carried out under an inert gas or hydrogen environment to avoid further oxidization of nanoparticles into other phases of iron oxide (*e.g.* γ-Fe_2O_3) [19]. Therefore, the microwave plasma-enhanced chemical vapor deposition (MW-PECVD) chamber was used, and hydrogen plasma was generated at a constant temperature of 600 °C for 10 min. This completely evaporated the organic material, and the nanoparticles could be imaged using scanning electron microscopy (SEM; Fig. 5a and b). Notably, significant patterning in the particle distribution was seen. Fig. **5**a shows the nanoparticles forming parallel strips due to the parallel patterned substrate surface left from the ion plating method (which is commonly used to coat commercial stainless steel [20]). A lower-magnification image (Fig. 5b) shows the collective effect of this process over a larger area. Despite the overall even distribution, some aggregations (bright dots) in the larger field-of-view image (Fig. 6) could be seen, which might be induced by lumps of organic materials in the aggregates (indicated with arrows in the TEM image of Fig. 1).

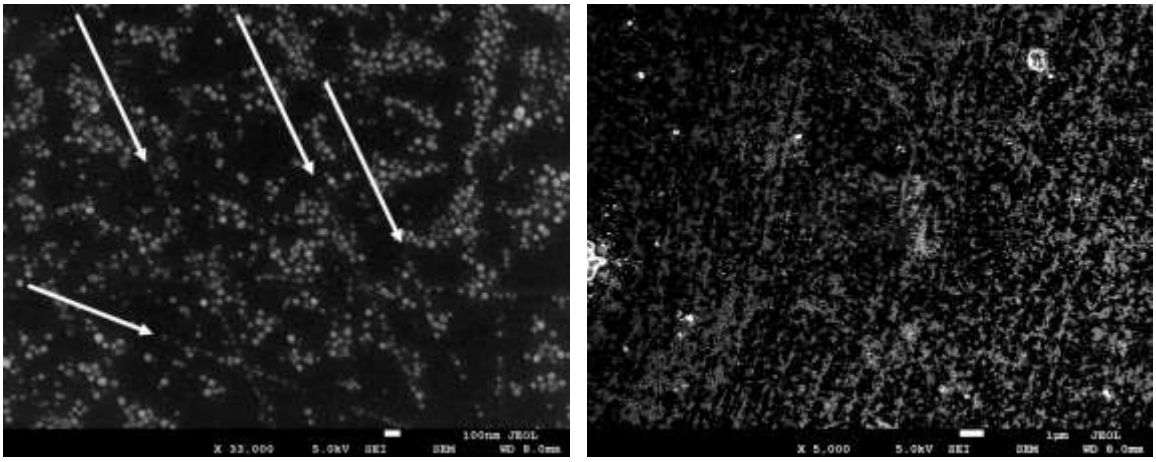

(a) (b)

Fig. 5 SEM images of deposited Fe_3O_4 nanoparticles. a Alignment of nanoparticles with the straight patterned lines formed by the ion plating techniques. **b** Collective effect of straight strips of particles over a larger area.

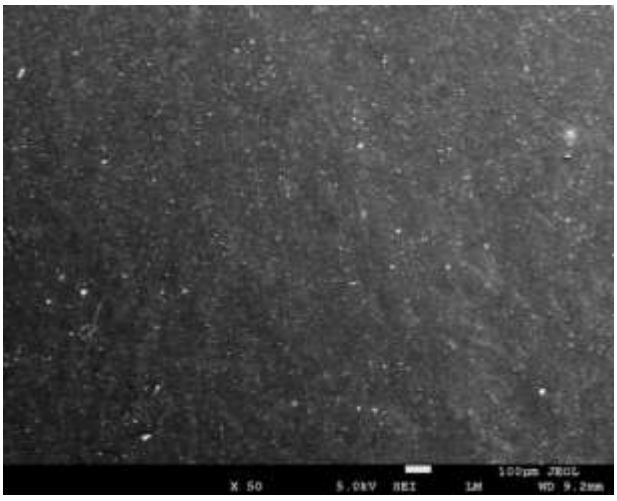

Fig. 6 Magnetite nanoparticle distribution over the substrate. The bright dots present aggregations of nanoparticles that originate from organic material.

Growth and densification of CNTs. In this work, the CNTs grew in a tip growth mechanism, in which the catalyst particle stays at the upper end of the growing tube. Under this mechanism, the particles move in two degrees of freedom atop the CNT film during the growth: being lifted by the tubes and moving sideways. In the early stage (~ one minute of growth), the particle agglomerates are distributed in a random yet uniform manner over large areas (Fig. 7). The particle lumps (indicated by yellow arrows in Fig. 1 and shown in Fig. 6) are hypothesized to further aggregate and collect smaller particles as the tubes grow.

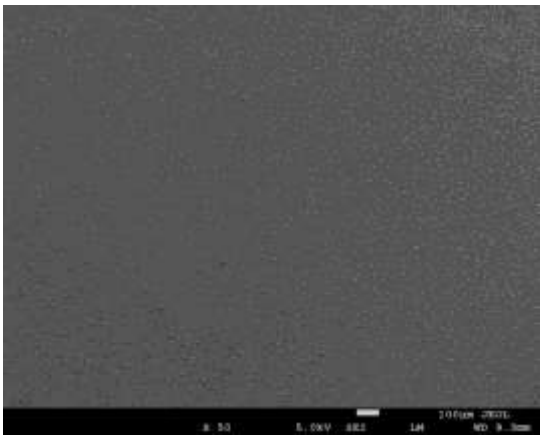

(a)

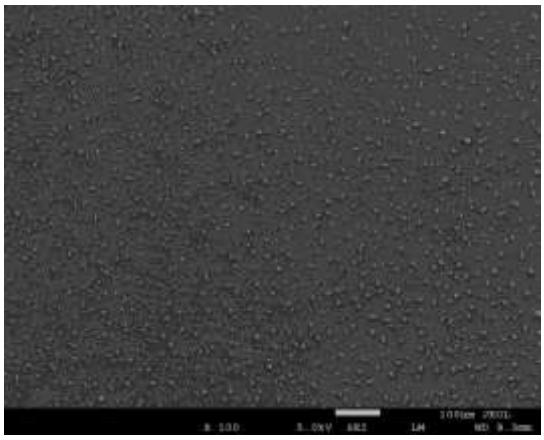

(b)

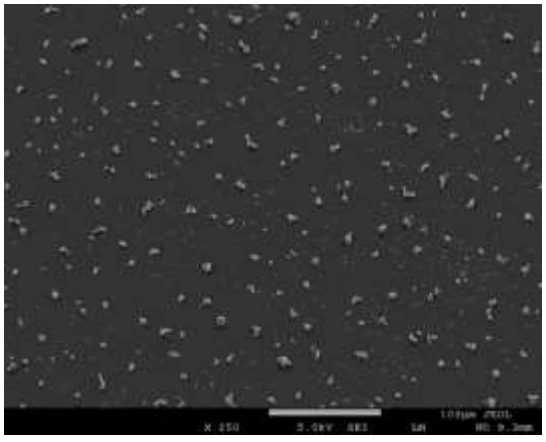

(c)

Fig. 7 Distribution of nanoparticles and their aggregation in the early stage (~ one minute of growth) at different magnifications.

The MW-CVD approach led to a highly reproducible pattern of the densification mechanism of CNTs during their growth. Fig. 8a–d show the top-view images of the grown CNT bundles at different magnifications. The average number of bundles per area is about 5×10^9 m^{-2}, which corresponds to an inter-bundle distance of about 14 μm. However, in principle, the site density of the bundles and hence the inter-bundle distance might be slightly changed by altering the concentration of particle suspension (not investigated here). Although the bundle centers are randomly distributed, their site density over a large area is roughly uniform. Another noticeable feature is the parallel lines that separate the bundles in some areas, which might result from the ion plating of the TiN coating as mentioned earlier [20]. This effect may serve as tools in the future to more precisely control the bundle distribution by patterning the substrate with coating. The tilted views (tile angle: 51.7° in Fig. 9) suggest that the bundle height was about 17 μm.

The Raman spectrum of the nanotubes using the 532 nm excitation is shown in Fig. 10. The characteristic peaks of MW-CNTs appear at 1567, 1332, and 2667 cm^{-1}. The first peak, known as the G band, corresponds to the in-plane vibrational mode of the carbon-carbon bond in the graphite structure. The disorders and dislocations contribute to the second peak known as the D band. The small peak at 2667 cm^{-1} is called the 2D band or the G' band, which is associated with the overtone of the disorders [21]. It is important to mention that the ratio of the two peaks' intensities I_G/I_D reveals low quality of the grown nanotubes. However, in principle, such characteristic can be further improved in future work by altering growth parameters.

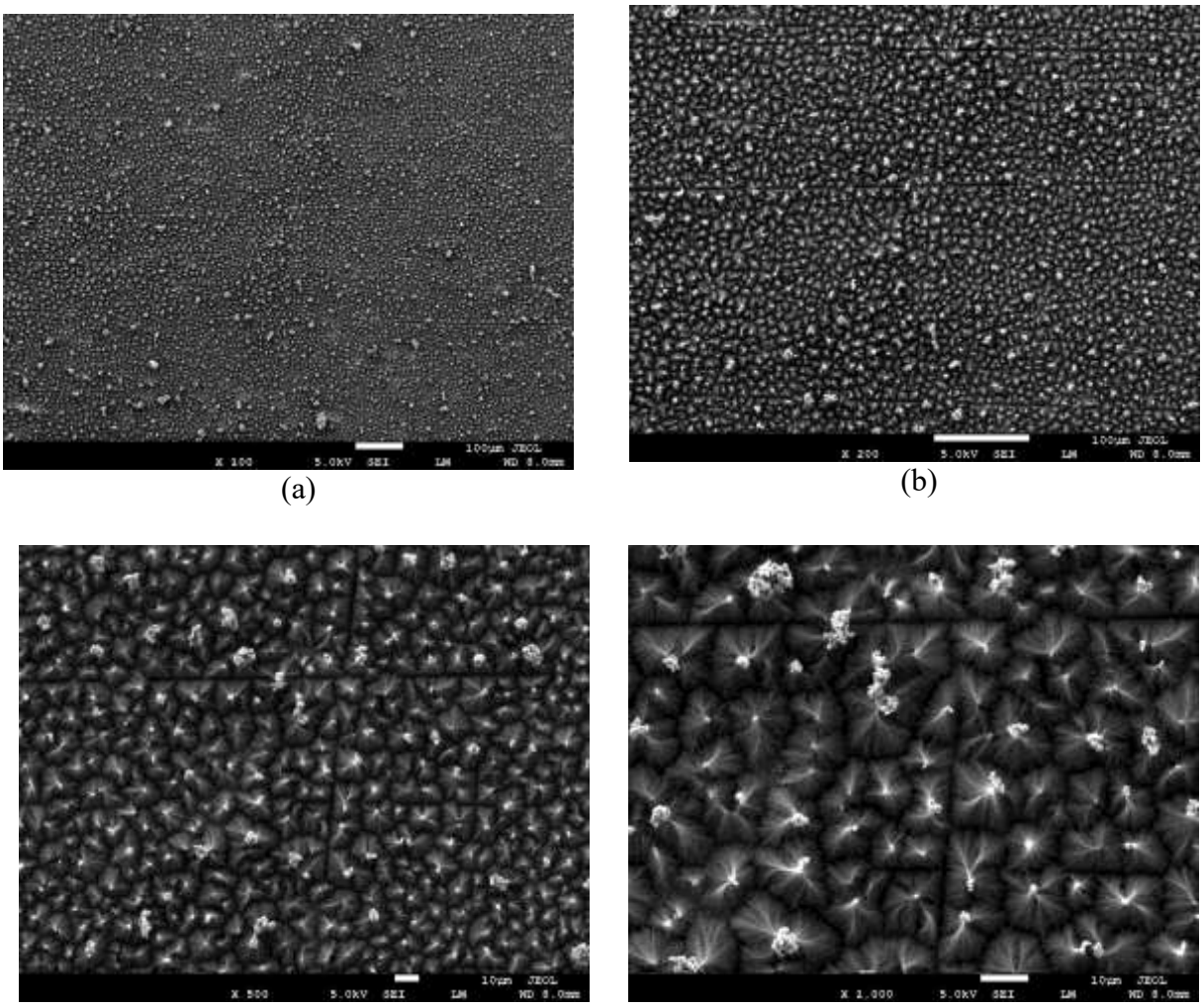

Fig. 8 Top-view SEM images of CNT film at different magnifications.

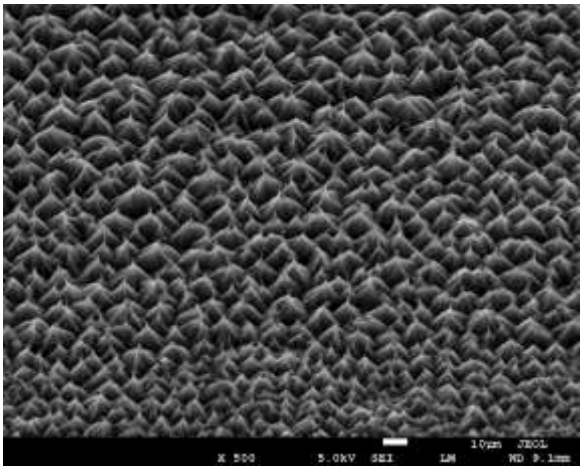

(a)

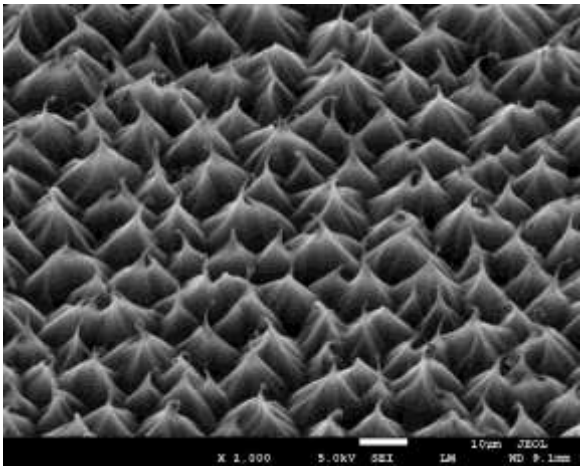

(b)

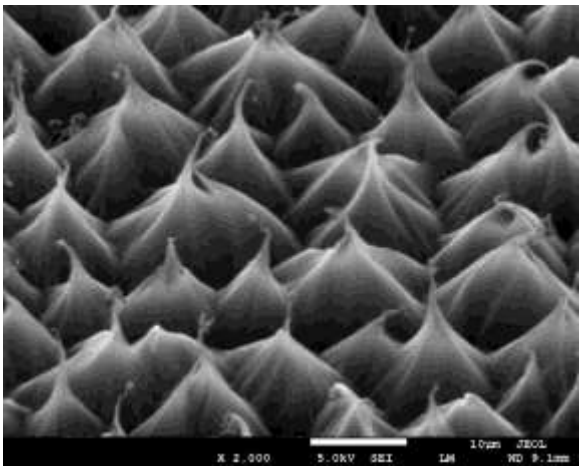

(c)

Fig. 9 Tilted-view SEM images of the grown CNTs at different magnifications.

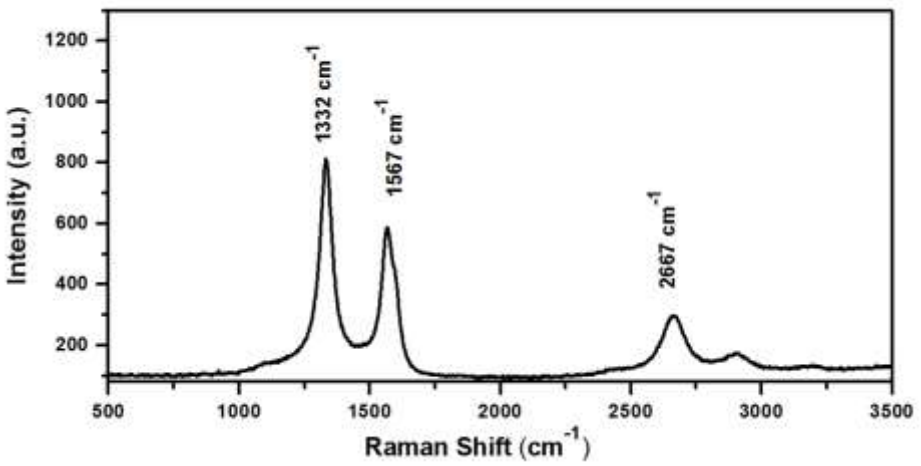

Fig. 10 Raman spectrum of nanotube bundles. The following main characteristic CNT peaks are visible: the G band (1567 cm^{-1}), D band (1332 cm^{-1}), and 2D band (2667 cm^{-1}).

The Raman spectrum does not provide conclusive evidence for the growth of MW-CNTs as graphite could also give similar results. To further investigate this, TEM was used to measure the tube diameter and number of walls. Fig. **11** presents two TEM images of the grown CNTs. The low-magnification image (Fig. 11a) provides a large field of view with a dense collection of nanotubes, where the even size of catalyst particles led to a narrow distribution of tube diameters. The average inner and outer diameters are about 10.5 and 14 nm, respectively, as seen from Fig. 11b, and fewer than 10 walls were counted (see the magnified inset).

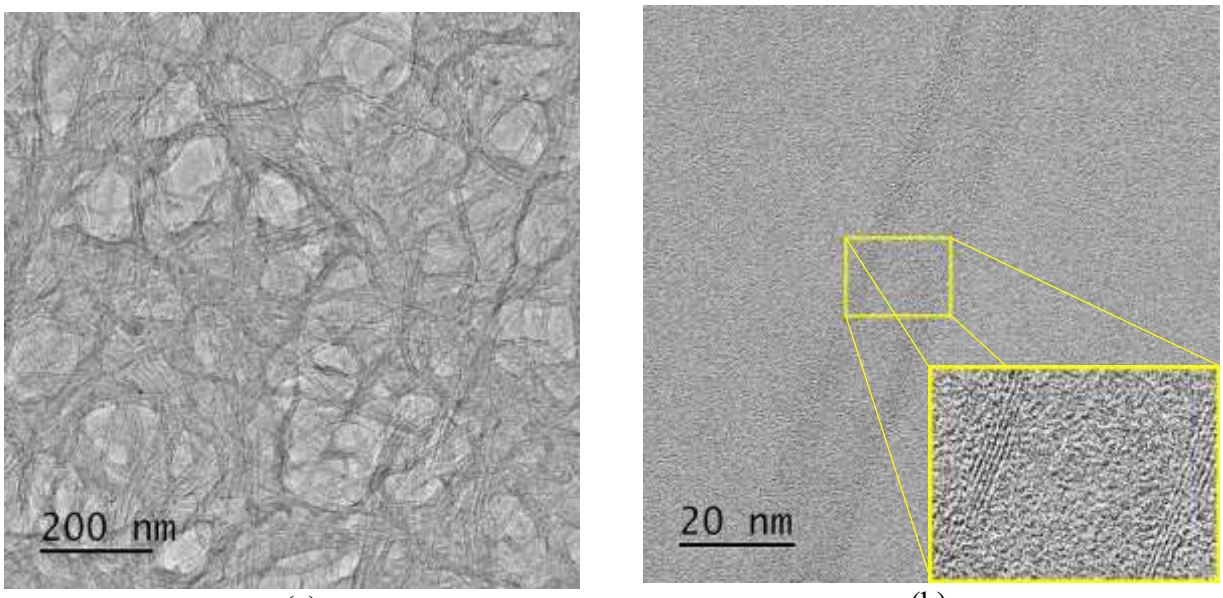

(a) (b)

Fig. 11 TEM images of the MW-CNTs. **a** Low-magnification image showing the narrow distribution of nanotube diameters. **b** High-magnification image of an individual nanotube.

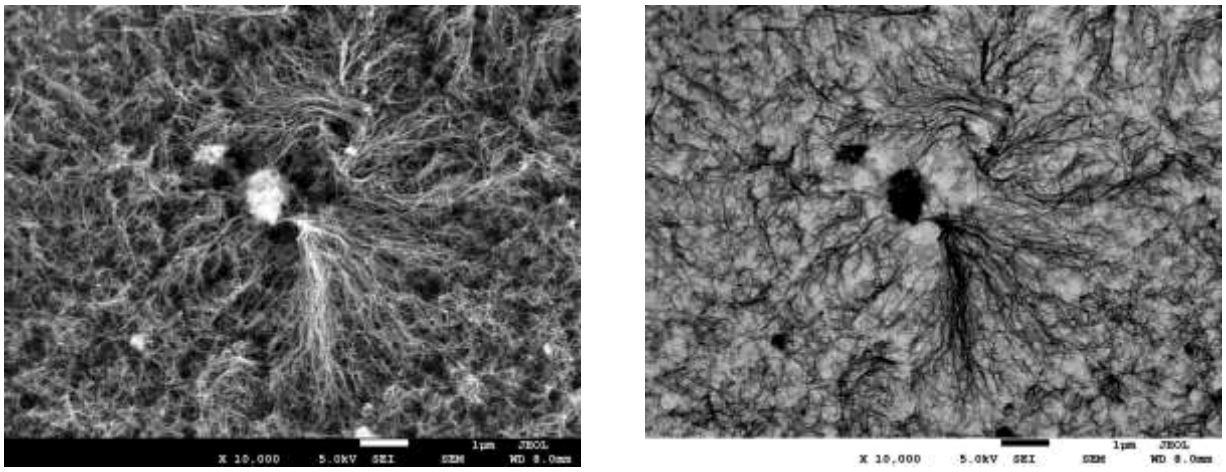

(a) (b)

Fig. 12 SEM images taken in the early growth stage. a Start of densification and **b** an inverted contrast image of the same area.

Although densification during tube growth experiments is highly reproducible in our experiments, the underlying mechanism is not fully understood yet. The following observations may offer some clue. The first observation is the collective behavior of the nanotube tips during their growth. Fig. 12a shows the early stage of densification during CNT growth, and Fig. 12b is an inverted image of the same area. As mentioned earlier, the nanotubes grow in a tip growth mechanism, with the catalyst particle located at the top of the vertically grown nanotube. As seen from Fig. 12a and b, the tube tips are slightly tilted in a way to allow smaller particles to be attracted to the larger aggregates. From the same images, we can see that this attraction is a special in a way that the particles at the nanotube heads do not take direct shortcuts towards the bigger particle. Alternatively, they move in a way that require them to align together in the same path first. Even the grown densified bundles show that the smaller top aggregations are attracted by the larger ones similarly. To emphasize this observation, we imaged an area close to the substrate edge, which tends to be more strongly affected by gradients in temperature and plasma intensity and therefore has different growth rates. Two regions of interest are outlined and labeled

1 and 2 in Fig. 13a and b. The number of particle aggregates was counted using the particle counter feature in ImageJ software. At an early stage of growth at region 1, the number of particles is 116 with an average particle size of 72 pixels. In region 2 having more advanced growth, 29 particles with an average size of 260 pixels are observed. Comparing regions 1 and 2, evidently there is an attraction force between the neighboring aggregations, which results in a local collective mechanism during the growth. Another significant observation is a strong helical twist of the peaks when they get closer to each other. Fig. 14a is a top-view image of the CNT bundles where local peak centers are collected together. Fig. 14b is a side-tilted view of bundle heads twisted around each other in a helical shape, which might originate from an alignment process.

Possible densification mechanism. The above observations might suggest that a magnetic dipole-dipole interaction is responsible for the collective process that gathers the heads of the bundles together. It is important mention that the relatively low CNTs site density in our experiment facilitates the freedom for nanotube densification through dipole-dipole interaction. In other words, if the site density of the tubes was high, crowd effect would occur resulting in a forced vertical alignment of the tubes. Since the catalyst particles are magnetic (Fe_3O_4), this dipole-dipole interaction might have been present even during particle deposition as the solvent evaporated [22]. The dipole-dipole potential between two particles i and j can be written as

$$V_{ij}^{DD} = -\frac{3(\boldsymbol{m}_i \cdot \hat{r}_{ij})(\boldsymbol{m}_j \cdot \hat{r}_{ij}) - \boldsymbol{m}_i \cdot \boldsymbol{m}_j}{4\pi\mu_\circ r_{ij}^3}$$

where m_i and m_j are the magnetic moments of particles i and j, $\mu_\circ$ is the permeability of free space, r_{ij} is the distance between i and j, and $\hat{r}$ is the unit vector pointing from i to j [22]. In the simplest case of only two magnetic particles, this interaction should cause the attraction and

alignment of their magnetic moments. If one particle is much more massive, we would expect the smaller one to be quickly drawn to the larger one while turning its dipole for alignment. In the case of a particle suspension, there will be local agglomerations everywhere due to the competing dipole-dipole interaction and Brownian motion [23].

To further understand the densification mechanism, TEM was used to explore the catalyst distribution in the bundle head. Fig. 15 presents four TEM images of a nanotube bundle. Fig. 15a is a low-magnification image covering the entire bundle. The aggregated catalyst heads consisting of large particles can be seen in Fig. 15c. The average size of our as-synthesized particles is about 20 nm. The large particles in these TEM images could have formed due to either heat centering or particle attraction during the growth (see Fig. 1). Complementary information from an SEM image of the catalyst heads (Fig. 16) supports the hypothesis of attraction as nanoparticles of ~20 nm size surrounded the large aggregations without affecting their shapes by the heat. Fig. 15b shows a dense nanotube bundle, and the area outlined by yellow rectangle is magnified in Fig. 15d. Some small catalyst particles are seen to be trapped within the tube bundle as the tubes gather in the tip during their growth.

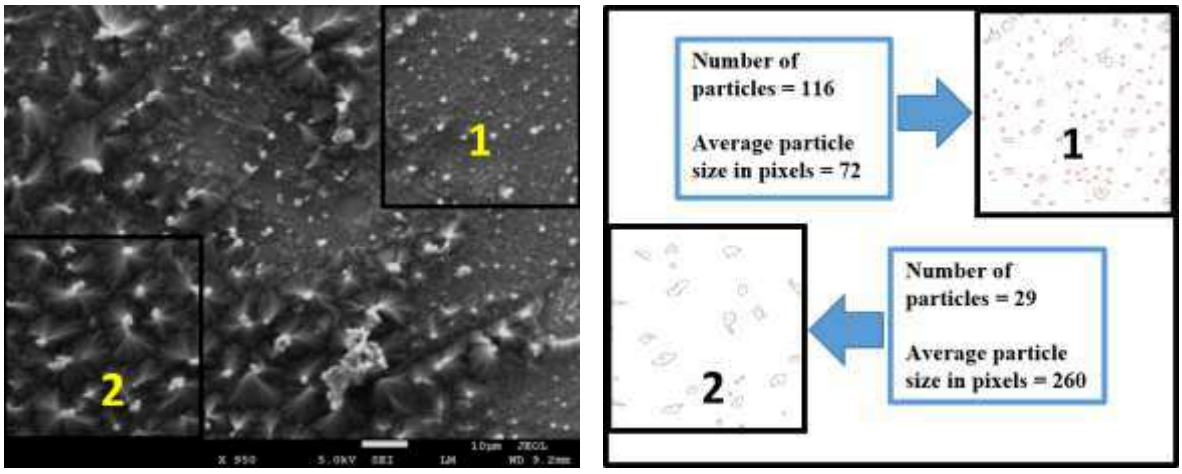

(a) (b)

Fig. 13 Particle growth in two regions of interest. a SEM image of the two areas with (1) initial growth and (2) advanced growth. **b** Top aggregations of the bundles counted using ImageJ.

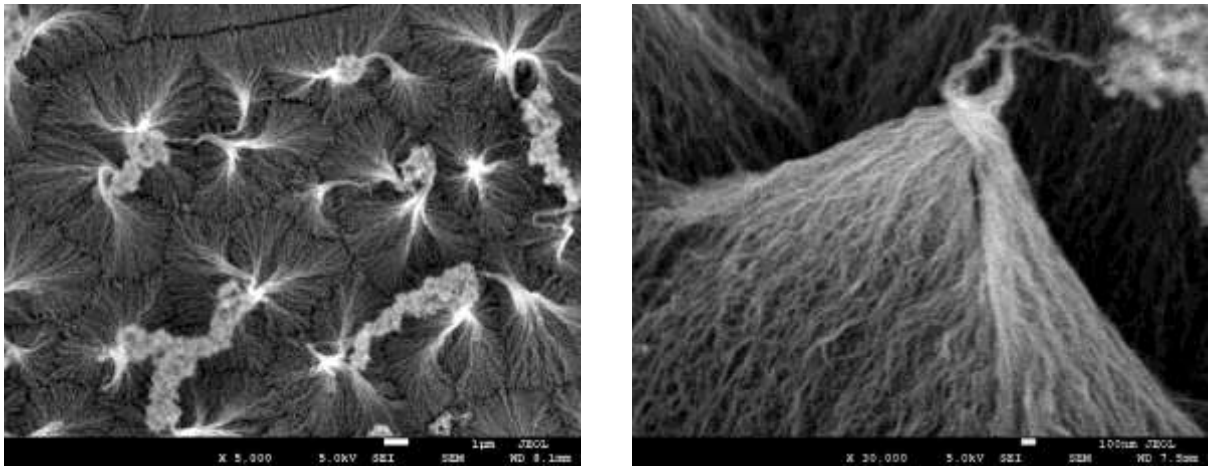

(a) (b)

Fig. 14 Twisting of the nanotubes during growth. a SEM image of bundles showing the twisted collective process of the heads. **b** A tilted image illustrating the helical twist.

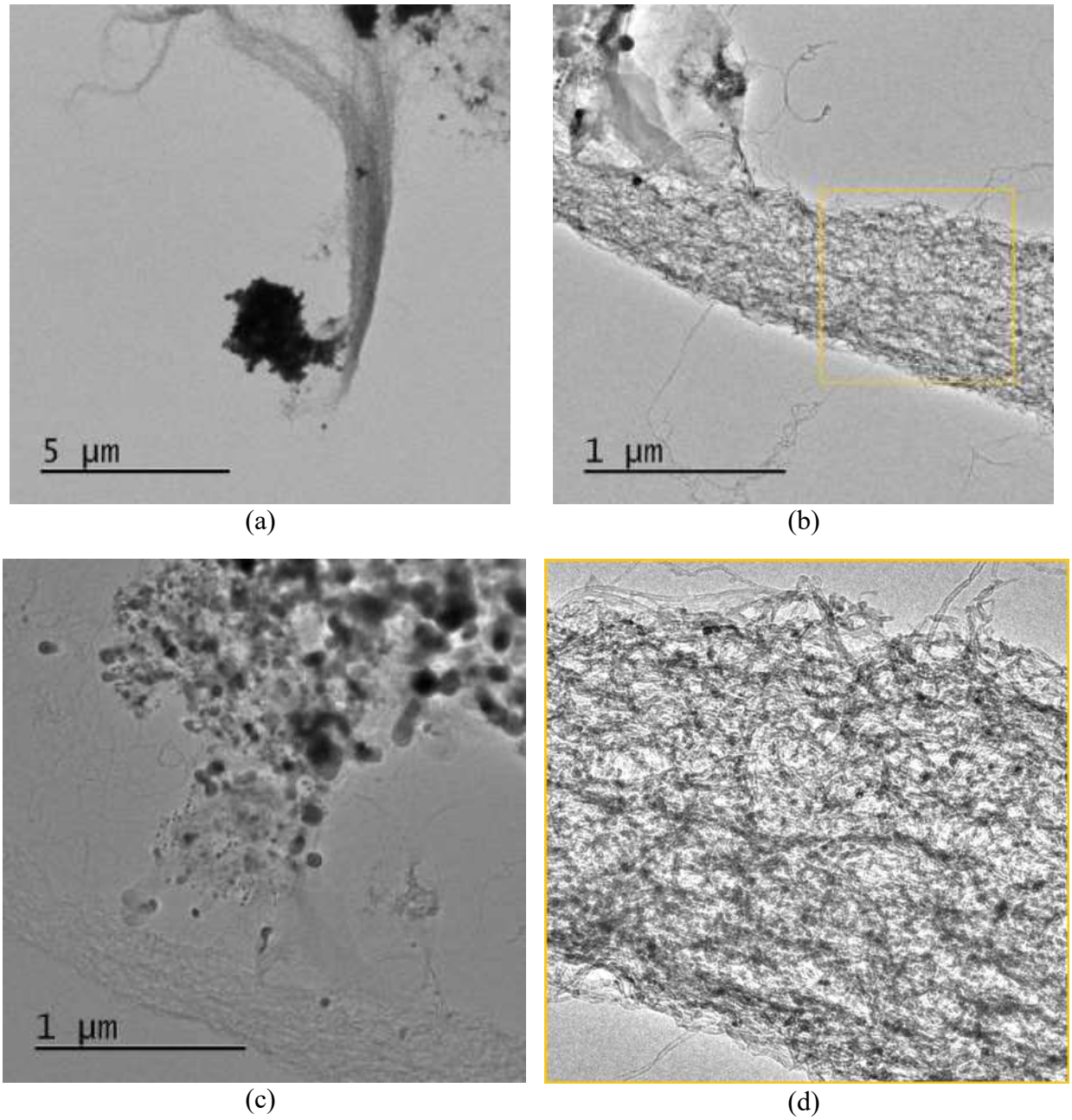

Fig. 15 TEM images of the top of the bundles. a Wide field view showing the entire bundle with the head catalyst aggregation. **b** Densified CNT bundle. A zoomed-in image of **c** the aggregation head and **d** densified tubes, showing the catalyst particles in a tip growth mechanism.

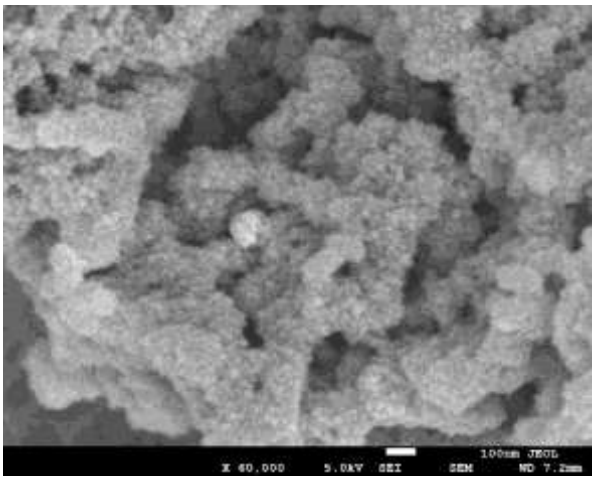

(a)

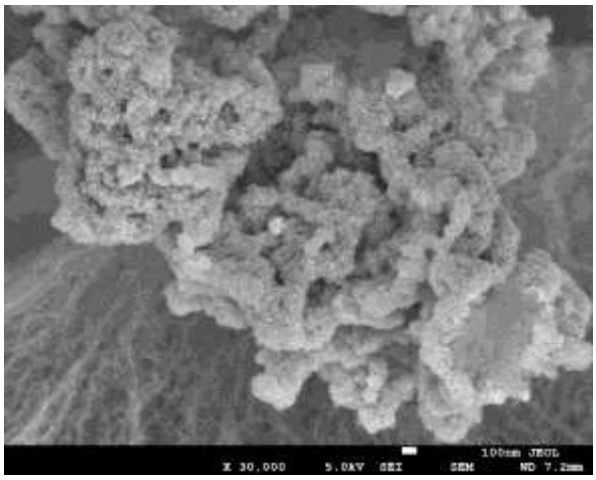

(b)

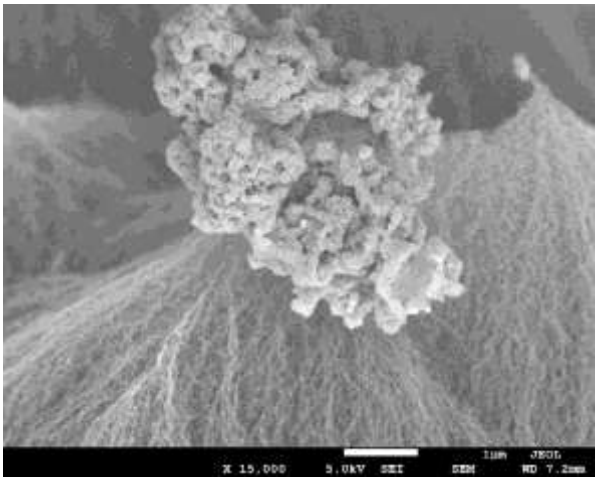

(c)

Fig. 16 SEM images of a bundle head. The head is a large aggregation of 20-nm nanoparticles.

It is important to mention that the collective magnetic mechanism is just one cause of the mutual attraction between catalyst particles, which led to the collection of tube tips. The Van der Waals force is another important force that comes into play when the tube walls touch each other. In other words, the final bundle structure is due to a combination of two forces: the magnetic dipole-dipole interaction starts the process, and then the Van der Waals force takes over.

CONCLUSIONS

In this work, we reported a novel mechanism for the densification of MW-CNTs into bundles during their growth. Utilizing colloidal catalysts and microwave plasma-enhanced CVD, we grew the CNT bundles in a highly reproducible manner. The key advantage of our method is to cost-effectively realize densification of nanotubes during growth. Further detailed observations suggest that magnetic dipole-dipole interaction among catalyst nanoparticles in the tip growth mechanism might drive the tubes to the center of larger aggregations with strong magnetic moments. After the tube walls approach each other, Van der Waals force contributes to the final CNT bundles structure. However, this study is only qualitative, and future work is required to quantitatively investigate effects from the substrate type, colloidal suspension concentration, particle size, method of particle deposition, and CNT growth conditions.

METHODS

Materials and synthesis. The colloidal catalyst nanoparticles were synthesized by thermal decomposition of iron carbonyl in octyl ether solvent, similar to this study [16]. Briefly, 1.28 g of oleic acid was dissolved in 10 mL of octyl ether, and the solution was heated on a hot plate and stirred. When the temperature stabilized temporarily at 100 °C, 0.2 mL of iron carbonyl was added. The resultant yellowish solution was heated gradually at about 300 °C for 1 h to reflux. At that point, the color turned to black, which suggests the formation of Fe_3O_4 nanoparticles. The black particle suspension was centrifuged, washed with ethanol, and then dispersed in hexane.

For the growth of CNTs, a commercially available TiN-coated stainless-steel sheet (thickness: 0.7 mm) was cut into squares (1 cm × 1 cm) as substrates. They were placed at the bottom of a beaker, and the catalyst particle suspension (0.033 mg/mL or 10^{12} particle/cm^3) was poured until

the substrate was just covered at 1 mm. The beaker was exposed to the environut at room temperature until all the hexane evaporated, resulting in a coat of particles on the substrate surface of site density ~ 945 particle/μm^2. The substrate was then placed in a microwave plasma-enhanced chemical vapor deposition (MW-PECVD) chamber (HPMS-2020, Chengdu Newman-Hueray Microwave Tech. Co., Ltd., China), and heated using H_2 plasma at 600 °C for 10 min at 7 kPa of pressure, 1000 W of microwave power, and 100 sccm flow rate of hydrogen gas. This was followed by the growth step where methane was introduced to the chamber at a flow rate of 20 sccm for another 10 min, while keeping other parameters unchanged.

Instrumentation. FE-SEM (JSM-7600F, JEOL) was employed to image the particle-covered substrate before and after CNT growth. High-resolution TEM (JEOL-JSM-200 KV-Japan) was used to confirm the particle size and their crystallinity, nanotube diameter and the number of walls therein, and catalyst-tubes structure. A Raman spectrometer (DXR Raman microscope, Thermo Fisher Scientific, USA) was employed to confirm the graphitic and dislocation modes of the grown CNTs and verify the phase of Fe_3O_4 nanoparticles. The crystalline structure of these nanoparticles was explored using X-ray diffraction (XRD; X'pert Pro).

Data availability

The authors declare that all data supporting the findings of this work are available from the corresponding authors upon reasonable request.

References

1. Iijima, S. Helical microtubules of graphitic carbon. *Nature* **354**, 56–58 (1991).

2. Meyyappan, M. *Carbon Nanotubes: Science and Applications*. (CRC Press: Boca Raton, 2004).

3. Salvetat, J. P. et al. Mechanical properties of carbon nanotubes. *Appl. Phys. A.* **69**, 255–260 (1999).

4. Schadler, L. S. & Zhao, Y. Ultrafast optical switching properties of single-wall carbon nanotube polymer composites at 1.55 μm. *Appl. Phys. Lett*. **81**, 975 (2002).

5. De Volder, M. F. L., Tawfick, S. H., Baughman, R. H. & Hart, A. J. Carbon nanotubes: Present and future commercial applications. *Science* **339**, 535–539 (2013).

6. De Heer, W. A., Chatelain, A. & Ugarte, D. A carbon nanotube field-emission electron source. *Science* **270**, 1179–1180 (1995).

7. Wang, Q. H., Yan, M. & Chang, R. P. H. Flat panel display prototype using gated carbon nanotube field emitters. *Appl. Phys. Lett.* **78**, 1294–1296 (2001).

8. Sugie, H. et al. Carbon nanotubes as electron source in an X-Ray tube. *Appl. Phys. Lett.* **78**, 2578–2580 (2001).

9. Dong, L., Arai, F. & Fukuda, T. Electron-beam-induced deposition with carbon nanotube emitters. *Appl. Phys. Lett.* **81**, 1919–1921 (2002).

10. Bocharov, G. & Eletskii, A. Theory of carbon nanotube (CNT)-based electron field emitters. *Nanomaterials* **3**, 393–442 (2013).

11. Liu, H., Kato, S. & Saito, Y. Empirical expression for the emission site density of nanotube film emitters. *Nanotechnology* **20**, 275206 (2009).

12. Zhu, L. et al. Growth and electrical characterization of high-aspect-ratio carbon nanotube arrays. *Carbon N. Y.* **44**, 253–258 (2006).

13. Wang, T., Jeppson, K. & Liu, J. Dry densification of carbon nanotube bundles. *Carbon N. Y.* **48**, 3795–3801 (2010).

14. Lim, Y. D. et al. Enhanced field emission properties of carbon nanotube films using densification technique. *Appl. Surf. Sci.* **477**, 211–219 (2017).

15. Correa-Duarte, M. A. et al. Fabrication and biocompatibility of carbon nanotube-based 3D networks as scaffolds for cell seeding and growth. *Nano Lett.* **4**, 2233–2236 (2004).

16. Hyeon, T., Lee, S. S., Park, J., Chung, Y. & Na, H. B. Synthesis of highly crystalline and monodisperse maghemite nanocrystallites without a size - selection process. *J. Am Chem. Soc.* **123**, 12798–12801 (2001).

17. Li, Z. et al. Solvothermal synthesis of nitrogen-doped graphene decorated by superparamagnetic Fe3O4 nanoparticles and their applications as enhanced synergistic microwave absorbers. *Carbon N. Y.* **115**, 493–502 (2017).

18. de Faria, D. L. A., Silva, S. V. & de Oliveira, M. T. Raman microspectroscopy of some iron oxides and oxyhydroxides. *J. Raman Spectrosc.* **28**, 873–878 (1997).

19. Gallagher, K. J., Feitknecht, W. & Mannweiler, U. Mechanism of oxidation of magnetite to γ-Fe2O3. *Nature* **217**, 1118–1121 (1968).

20. Prokudina, V. K. Titanium Nitride. In *Concise Encyclopedia of Self-Propagating High-Temperature Synthesis* (eds. Borovinskaya, I. P. et al.) 398–401 (Elsevier: Amsterdam, 2017).

21. Jorio, A., Dresselhaus, M. S., Saito, R. & Dresselhaus, G. *Raman Spectroscopy in Graphene Related Systems* (Wiley VCH Verlag: Weinheim, 2011).

22. Huke, B. & Lucke, M. Magnetic properties of colloidal suspensions of interacting magnetic particles. *Rep. Prog. Phys.* **67**, 1731 (2004).

23. Wang, Z., Holm, C. & Müller, H. W. Molecular dynamics study on the equilibrium magnetization properties and structure of ferrofluids. *Phys. Rev. E* **66**, 021405 (2002).

Acknowledgments

This project was funded by the Deanship of Scientific Research (DSR), King Abdulaziz University, Jeddah, under grant no. D-184-130-1440. The authors, therefore, gratefully acknowledge the DSR technical and financial support.

Author contributions

Dr. Alzahrani carried out most of the work by proposing the experiment, analyzing data, deriving the conclusions, and writing up the manuscript. Together with Dr. Alzahrani, Mr. Alayash contributed mainly to the preliminary experiments and observed the first successful bundle formation. Mr. Alghamdi synthesized the magnetic nanoparticles, worked with Mr. Alayash in a large portion of the experimental work, and helped with data analysis and graphing. All authors have given approval to the final version of the manuscript.

Competing interests

The authors declare no competing interests.

Supplementary Files

This is a list of supplementary files associated with this preprint. Click to download.

- GraphicalAbstractScientificreports.tif